

# Exploring the performance of a vibro-impact energy harvester under asymmetric restitution coefficients

Yuyao Jiang  
27803080

Department of Mathematics and Statistics  
University of Reading

March 4, 2022

## Abstract

A two-sided vibro-impact energy harvester under asymmetric restitution coefficients can effectively convert the kinetic energy of a ball's motion into electrical energy in the form of output voltage. The principle is that the collision from the ball deforms the membranes and then deformed membranes convert kinetic energy into electrical energy that can be collected due to the special material of membranes. The material is an electrically active polymer - dielectric elastomer, which is sandwiched between two electrodes organising a capacitor with variable capacitance. The amount of collected energy at per impact through the deformation quantity of the membrane can be observed and quantified through the average output voltage. We firstly characterize the parameters of the model, analyze the two types of T-periodic motions which are from bottom to top and from top to bottom, then get the analytical solutions and conduct linear stability analysis with asymmetric restitution coefficients for the triples  $(\dot{Z}_k, \phi_k, \Delta t_k)$ . Our aim is to figure out what is the optimal energy harvester in terms of dynamics that will harvest maximum energy through numerical simulations. Based on the previous results, we focus on the conditions with asymmetric restitution coefficients and test the amount of energy generated by different combinations of restitution coefficients with the same angle of incline, then the average voltage output under different cases is compared in energy harvesting diagram and some useful conclusions have been drawn. After that, the influence of angles of incline is taken into account. To better understand various types of behaviors, two typical motions 1-1 T-periodic motion and 2-1 T-periodic motion are singled out and analyzed analytically and numerically through bifurcation diagrams, phase portraits and velocity time series.

**Keywords** - Vibro-impact energy harvesting, T-periodic motion, linear stability analysis, bifurcation diagram, maximum energy output

## Contents

<b>List of Tables</b>	<b>ii</b>
<b>List of Figures</b>	<b>ii</b>
<b>1 Introduction</b>	<b>1</b>
<b>2 The vibro-impact energy harvesting model and previous results</b>	<b>2</b>
2.1 Parametric characterizations of T-periodic motion . . . . .	2
2.2 Analytical results for T-periodic motion with $r_T \neq r_B$ . . . . .	4
2.3 Linear stability analysis for T-periodic motion with $r_T \neq r_B$ . . . . .	5
<b>3 Influence of parameters on energy harvesting</b>	<b>6</b>
3.1 Influence of restitution coefficients $r$ under $\beta = \pi/6$ . . . . .	6
3.2 Influence of angle of capsule incline $\beta$ . . . . .	8
<b>4 Different behaviors of bifurcation diagrams</b>	<b>10</b>
4.1 1-1 T-periodic motion . . . . .	11
4.2 2-1 T-periodic motion . . . . .	12
<b>5 Conclusions</b>	<b>12</b>
<b>6 Bibliography</b>	<b>14</b>
<b>A Appendix</b>	<b>16</b>

## List of Tables

1	Parameters and variables of the vibro-impact energy harvesting system . . .	3
2	Different combinations of restitution coefficients and angles of capsule incline	6

## List of Figures

1	Model of the vibro-impact energy harvester . . . . .	2
2	$r_B = 0.5, r_T = 0.5, \beta = \pi/6, v_{rel0} = 0.5293$ . . . . .	6
3	$r_B = 0.6, r_T = 0.3, \beta = \pi/6, v_{rel0} = 0.5293$ . . . . .	7
4	$r_B = 0.3, r_T = 0.6, \beta = \pi/6, v_{rel0} = 67$ . . . . .	7
5	$r_B = 0.5, r_T = 0.4, \beta = \pi/6, v_{rel0} = 0.5293$ . . . . .	8

6	$r_B = 0.4, r_T = 0.5, \beta = \pi/6, v_{rel0} = 23$ . . . . .	8
7	$r_B = 0.5, r_T = 0.5, \beta = \pi/3, v_{rel0} = 0.5293$ . . . . .	9
8	$r_B = 0.6, r_T = 0.3, \beta = \pi/3, v_{rel0} = 0.5293$ . . . . .	9
9	$r_B = 0.5, r_T = 0.4, \beta = \pi/3, v_{rel0} = 0.5293$ . . . . .	9
10	$r_B = 0.4, r_T = 0.5, \beta = \pi/3, v_{rel0} = 23$ . . . . .	10
11	Bifurcation diagram about relative velocity and $\phi$ . . . . .	11
12	Initial conditions: $ss(d) = 0.33, v_{rel0}(\dot{z}) = 0.729028, \phi_0(\phi) = 1.21387$ . .	11
13	Initial conditions: $ss(d) = 0.25, v_{rel0}(\dot{z}) = 0.689829, \phi_0(\phi) = 0.922985$ . .	12
14	Comparison of energy harvesting of all figures . . . . .	12

# 1 Introduction

Recently, wide application of mechanical devices driven by internal force have attracted experts in various fields to study how to maximize production capacity. In practical industrial applications, how to adjust each parameter of equipment to maximize the efficiency of production has become a common research problem. Many researchers have also proposed various models and energy conversion methods for that common purpose. The basic idea originally proposed by Chernous' Ko (2002) is that the rectilinear motion of a system can be engineered using a periodically driven internal mass interacting with the main body under dry friction force. For instance, a miniaturized medical capsule can move inside human body by adopting this method. In this way, many complications result from external driving mechanism, e.g. Glass et al. (2008), Valdastrì et al. (2009), can be effectively avoided. However, understanding of the dynamic process and reasonable analysis of such mechanism matters a lot and they have to be carefully analysed and designed for the system to improve the performance of energy harvesting.

Until the vibro-impact system was proposed, it can help us observe a wide range of rich nonlinear phenomena. Another advantage of this system is that it is conservative and keeps a constant energy level between each impact. As for the limitation of this design, most of the derived maps such as bifurcation diagrams and phase portraits can not be solved explicitly, which can only be treated semi-analytically and numerically. A special material called dielectric elastomer have been applied in the vibro-impact system with the potential to convert vibration energy to electricity. And the dielectric elastomer generator, first proposed by Pelrine et al. in Pelrine et al. (2001), consists of a variable capacitor made of highly deformable elastomeric material sandwiched between flexible electrodes Yurchenko, Lai, Thomson, Val & Bobryk (2017). Later a detailed vibro-impact energy harvesting model shown in Fig.1 that describes the different motions of energy harvesting was developed and the influence of the material dielectric coefficient on the energy harvesting performance and bias voltage was studied in Graf et al. (2014).

Previous analytical studies (Serdukova et al. (2021), Dulin et al. (2022)) have revealed some interesting conclusions about the vibro-impact energy harvesting model. For example, period doubling bifurcations and grazing transitions play a important role during the process of transitions between periodic solutions which are stable. However, this kind of transition can reduces the energy harvesting performance immediately, which is not beneficial for us. Besides, grazing is defined as an impact with zero velocity and grazing bifurcation can deteriorate the system performance, which can not deform the membrane and produce any power as a result.

The paper is organized as follows. In Section 2 we build a vibro-impact model for energy harvesting, characterize its parameters and discuss the analytical results for T-periodic motion with different restitution coefficients. In Section 3 we consider how much influence do restitution coefficients and angles of incline have on the average output voltage. The optimal combination of coefficients is obtained in the process. In Section 4 we give analytical and numerical analyses of two T-periodic motions in a particular case by observing bifurcation diagrams, phase portraits and velocity time series. In Section 5 we show the optimal device design with key conclusions drawn in the exploration process. The limitations of research methods and the direction of future improvement are also put forward.

## 2 The vibro-impact energy harvesting model and previous results

### 2.1 Parametric characterizations of T-periodic motion

A vibro-impact energy harvesting system shown in Fig.1 that has been proposed in [Yurchenko, Val, Lai, Gu & Thomson \(2017\)](#), [Yurchenko, Lai, Thomson, Val & Bobryk \(2017\)](#) is one of the most typical and attractive models of nonlinear dynamics, in which the absolute and relative motions of the ball and capsule can be observed and analytical solutions for output voltage and relative velocity can be obtained. However, the impact cannot be treated as ideally elastic due to the fact that the velocity of the system is discontinues in practical application, which makes the system difficult to be analysed ([Serdukova et al. \(2021\)](#)). To overcome the difficulty, a T-periodic motion of the vibro-impact energy harvester contains a capsule of mass  $M$  and length  $s$  with a ball of mass  $m$  moving inside it.  $\ddot{X}(\tau)$  represents capsule acceleration,  $\ddot{x}(\tau)$  represents ball acceleration and  $\dot{x}^+ = -r\dot{x}^- + (r+1)\dot{X}$  is the impact condition which is used to calculate the velocity of the ball after an impact. Concerning about how energy production happens, according to method proposed in [Serdukova et al. \(2021\)](#), [Strogatz \(2018\)](#), the impacts deform the membrane and then drive the ball motion. Especially the membrane is made of dielectric elastomer (DE), which is sandwiched between two electrodes organising a capacitor with variable capacitance. Therefore the maximum energy absorption by the ball happens when both masses are anti-phased. Some parameters and variables of the vibro-impact energy harvesting system are shown in Table 1.

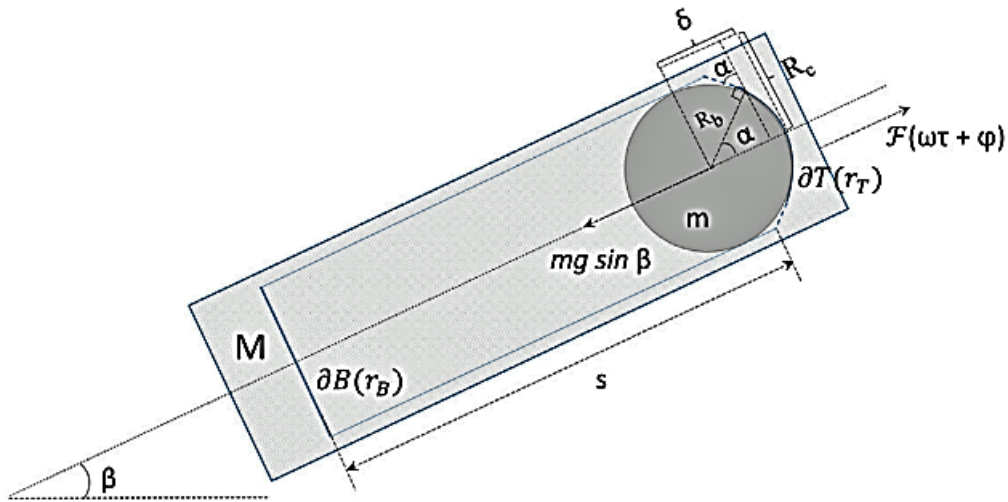


Figure 1: Model of the vibro-impact energy harvester

Parameters	Description
$M=124.5\text{g}$ ( $m=3.5\text{g}$ )	Mass of the capsule (ball)
$\beta$	Angle of capsule incline
$d$ (s)	Non-dimensional (Dimensional) capsule length
$\hat{F}(w\tau + \phi)$	A harmonic excitation with period $\frac{2\pi}{w}$
$A =   \hat{F}   = 1$	Excitation amplitude $\hat{F}$
$r_B(r_T)$	Restitution coefficient for the bottom (top)
$g = 9.8\text{m/s}^2$	Acceleration of gravity
$U_{in} = 2000\text{V}$	Rated input voltage
$R_b = 5\text{mm}$	Radius of the ball
$R_c = 6.3\text{mm}$	Radius of the undeformed membrane
$K = 4.0847 \cdot 10^5, v = 2.6$	Parameters of the elastic force of the membrane

Table 1: Parameters and variables of the vibro-impact energy harvesting system

The results that have been presented in [Yurchenko, Val, Lai, Gu & Thomson \(2017\)](#), [Yurchenko, Lai, Thomson, Val & Bobryk \(2017\)](#) are used to write Matlab code.

The motion of the capsule is

$$\ddot{X}(\tau) = \frac{\hat{F}(w\tau + \phi)}{M} \quad (1)$$

The motion of the ball is

$$\ddot{x}(\tau) = -g \sin \beta \quad (2)$$

The relative velocity at the  $k$ th impact is

$$\dot{Z}(t) = -r\dot{Z}^-(t_k) + \bar{g}(t - t_k) + F_1(t) - F_1(t_k) \quad (3)$$

The relative position at the  $k$ th impact is

$$Z(t) = Z_k^- - r\dot{Z}_k^-(t - t_k) + \frac{\bar{g}}{2}(t - t_k)^2 + F_2(t) - F_2(t_k) - F_1(t_k)(t - t_k), \quad (4)$$

where  $F_1(t) = \int f(t)dt$  and  $F_2(t) = \int F_1(t)dt$

The voltage generated by the membrane deformation at the  $k$ th impact is

$$U_k^{imp} = \left[\frac{A_k}{\pi R_c^2}\right]^2 U_{in}, \quad (5)$$

where  $A_k$  is the area of the membrane at the deformed state and  $R_c$  is radius of the undeformed membrane.

The absolute output voltage at the  $k$ th impact is

$$U_k = U_k^{imp} - U_{in} \quad (6)$$

The average per impact output voltage is

$$\bar{U}_I = \frac{\sum_{k=1}^N U_k}{N} \quad (7)$$

## 2.2 Analytical results for T-periodic motion with $r_T \neq r_B$

By evaluating the relative velocity (3) and position (4) under successive impact with asymmetric  $r_T \neq r_B$ , we firstly introduce four basic nonlinear maps:

$$P_1 : \partial B \mapsto \partial T, P_2 : \partial T \mapsto \partial B, P_3 : \partial B \mapsto \partial B, P_4 : \partial T \mapsto \partial T \quad (8)$$

$P_1$  corresponding to the motion from the bottom of the capsule ( $\partial B$ ) to the top ( $\partial T$ ), and  $P_2$  representing the transition from the top of the capsule ( $\partial T$ ) to the bottom ( $\partial B$ ). Here we just focus on 1-1 T-periodic motion composed of the alternating maps  $P_1$  and  $P_2$ .

We get these algebraic expressions below which have been proposed in [Dulin et al. \(2022\)](#) and operationalize them in Matlab.

The time between the impacts is  $T_1$  for  $P_1 : \partial B(t_k) \mapsto \partial T(t_{k+1})$ , and  $T_2$  for  $P_2 : \partial B(t_{k+1}) \mapsto \partial T(t_{k+2})$ , where  $T_1 = \Delta t_k = t_{k+1} - t_k$ ,  $T_2 = \Delta t_{k+1} = t_{k+2} - t_{k+1}$ .

By the time evolution (3) and (4), we can derive the relative impact velocity  $\dot{Z}_j$  and the relative position  $Z_j$  from the previous velocity  $\dot{Z}_{j-1}$ ,

$$P_1: (Z_k \in \partial B, \dot{Z}_k, t_k) \rightarrow (Z_{k+1} \in \partial T, \dot{Z}_{k+1}, t_{k+1}),$$

$$\dot{Z}_{k+1} = -r_B \dot{Z}_k + \bar{g}T_1 + F_1(t_{k+1}) - F_1(t_k) \quad (9)$$

$$-d = -r_B \dot{Z}_k T_1 + \frac{\bar{g}}{2} T_1^2 + F_2(t_{k+1}) - F_2(t_k) - F_1(t_k) T_1 \quad (10)$$

$$P_2: (Z_{k+1} \in \partial T, \dot{Z}_{k+1}, t_{k+1}) \rightarrow (Z_{k+2} \in \partial B, \dot{Z}_{k+2}, t_{k+2}),$$

$$\dot{Z}_{k+2} = -r_T \dot{Z}_{k+1} + \bar{g}T_2 + F_1(t_{k+2}) - F_1(t_{k+1}) \quad (11)$$

$$d = -r_T \dot{Z}_{k+1} T_2 + \frac{\bar{g}}{2} T_2^2 + F_2(t_{k+2}) - F_2(t_{k+1}) - F_1(t_{k+1}) T_2 \quad (12)$$

According to the periodicity of the motion:

$$Z_{k+2} = Z_k, \dot{Z}_{k+2} = \dot{Z}_k, T = T_1 + T_2, f(t) = f(t + T), F_1(t) = F_1(t + T), F_2(t) = F_2(t + T) \quad (13)$$

From these we can obtain the triple  $(\dot{Z}_k, \phi_k, \Delta t_k)$ , which is the analytic solutions of 1-1 T-periodic motion. The  $k$ th impact at  $\partial B$  is set as the initial impact, then  $\dot{Z}_k$  is the relative impact velocity between the  $k$ th and the  $(k+1)$ th impact,  $\Delta t_k$  is the time between the  $k$ th and the  $(k+1)$ th impact, and  $\phi_k = \text{mod}(\pi t_k + \phi, 2\pi)$  is the phase shift of the  $k$ th impact. Adding (9) and (11), then using (9) and (13), we can get the first equation for  $\dot{Z}_k$ ,

$$\dot{Z}_k = \frac{1}{1 - r_B r_T} [\bar{g}T - (1 + r_T)(\bar{g}T_1 + F_1(t_{k+1}) - F_1(t_k))]. \quad (14)$$

By adding (10) and (12) and using (9) and (13), we get the second equation for  $\dot{Z}_k$ ,

$$\dot{Z}_k = \frac{1}{r_B T_1 - r_B r_T T_2} \left[ \frac{\bar{g}}{2} (T_1^2 + T_2^2) - r_T T_2 (\bar{g}T_1 + F_1(t_{k+1}) - F_1(t_k)) - F_1(t_k) T_1 - F_1(t_{k+1}) T_2 \right]. \quad (15)$$

By rewriting (10), we get the third equation for  $\dot{Z}_k$ ,

$$\dot{Z}_k = \frac{1}{r_B T_1} \left[ d + \frac{\bar{g}}{2} T_1^2 + F_2(t_{k+1}) - F_2(t_k) - F_1(t_k) T_1 \right]. \quad (16)$$

With the help of the *vpasolve* function in Matlab we can solve for the triple  $(\dot{Z}_k, \phi_k, \Delta t_k)$  using (14)(15)(16). To simplify the operations and form of the triple  $(\dot{Z}_k, \phi_k, \Delta t_k)$ , we choose the forcing  $f(t) = \cos(\pi t + \phi)$ .

### 2.3 Linear stability analysis for T-periodic motion with $r_T \neq r_B$

A linear stability analysis around the triple  $(\dot{Z}_k, \phi_k, \Delta t_k)$  is adopted to observe the linear stability for the solutions at critical points.

$\delta \mathbf{H}_k$  is taken to be a small perturbation of the fixed point  $\delta \mathbf{H}_k = (t_k, Z_k)$  corresponding to 1-1 T-periodic motion composed of the alternating maps  $P_1$  and  $P_2$ . The following equation for  $\delta \mathbf{H}_{k+2}$  can be obtained by linearizing about  $\delta \mathbf{H}_k = 0$ :

$$\delta \mathbf{H}_{k+2} = DP(\mathbf{H}_k^*) \delta \mathbf{H}_k = DP_2(\mathbf{H}_{k+1}^*) \cdot DP_1(\mathbf{H}_k^*) \delta \mathbf{H}_k, \quad (17)$$

Also

$$DP(\mathbf{H}_k^*) = DP_2(\mathbf{H}_{k+1}^*) \cdot DP_1(\mathbf{H}_k^*) = \begin{bmatrix} \frac{\partial t_{k+2}}{\partial t_{k+1}} & \frac{\partial t_{k+2}}{\partial \dot{Z}_{k+1}} \\ \frac{\partial Z_{k+2}}{\partial t_{k+1}} & \frac{\partial Z_{k+2}}{\partial \dot{Z}_{k+1}} \end{bmatrix}_{\mathbf{H}_{k+1}=\mathbf{H}_{k+1}^*} \cdot \begin{bmatrix} \frac{\partial t_{k+1}}{\partial t_k} & \frac{\partial t_{k+1}}{\partial \dot{Z}_k} \\ \frac{\partial Z_{k+1}}{\partial t_k} & \frac{\partial Z_{k+1}}{\partial \dot{Z}_k} \end{bmatrix}_{\mathbf{H}_k=\mathbf{H}_k^*}, \quad (18)$$

The entries of the matrix can be derived by differentiating (9)(10) with respect to  $t_k, \dot{Z}_k$  and (11)(12) with respect to  $t_{k+1}, \dot{Z}_{k+1}$ . These entries and trace  $Tr(DP)$  and determinant  $Det(DP)$  of the matrix  $DP$  are given in A Appendix. Then we can compute eigenvalues of the matrix  $DP$ :

$$\lambda_{1,2} = \frac{Tr(DP) \pm \sqrt{\Delta}}{2}, \quad \Delta = [Tr(DP)]^2 - 4 \cdot Det(DP) \quad (19)$$

Different stable and unstable behaviors are defined according to different ranges of parameters. According to [Serdukova et al. \(2021\)](#), if  $\Delta < 0$ , then  $\lambda_{1,2}$  are complex and the fixed point corresponds to a focus. If  $\Delta > 0$ , then  $\lambda_{1,2}$  are real and the fixed point corresponds to a node. As for the stability, the fixed point is stable with  $|\lambda| < 1$  and unstable with  $|\lambda| > 1$ . By observing the figures showing the relationship of relative velocity at  $t_k$  with respect to the capsule length  $d$ , we can find that in Fig.2 when  $d = 0.4$ , both two points  $(0.4, 0.83272)$  and  $(0.4, -0.67004)$  indicate transitions of the fixed point  $\mathbf{H}_k^*$  from a stable focus to a stable node happened in local behavior. When  $d = 0.26$ , points  $(0.26, 0.677449)$  and  $(0.26, -0.514769)$  indicate a period doubling bifurcation (instability) from 1-1 periodic solutions to 1-1 solutions with  $2T$ . In Fig.3 the points  $(0.26, 0.701752)$  and  $(0.26, -0.555468)$  indicate a grazing transition from 1-1 motion to 2-1 motion.

As for the energy collected at above points, in Fig.3 when solutions have a grazing transition from 1-1 to 2-1 motion, the average output voltage at  $(0.26, 27766.5)$  has a noticeable drop as the second impact in 2-1 motion has lower velocity compared with that in 1-1 motion. However, in Fig.2 the impact velocities do not change dramatically at the point  $(0.26, 37876.8)$  representing the period doubling of 1-1 solutions, so there is no dramatic drop in the average output voltage.



### 3 Influence of parameters on energy harvesting

The effect of restitution coefficients  $r_B$ ,  $r_T$  and angles of capsule incline  $\beta$  on energy collection will be investigated in detail. These parameters are set in several representative combinations shown in the Table 2 below. As for the ranges of other parameters are fixed like the capsule length  $d$  which is discussed in (0.1, 0.5), initial phase shift  $\phi = 6.18$ .

Figure	Parameters
2	$r_B = 0.5, r_T = 0.5, \beta = \pi/6, vrel0 = 0.5293$
3	$r_B = 0.6, r_T = 0.3, \beta = \pi/6, vrel0 = 0.5293$
4	$r_B = 0.3, r_T = 0.6, \beta = \pi/6, vrel0 = 67$
5	$r_B = 0.5, r_T = 0.4, \beta = \pi/6, vrel0 = 0.5293$
6	$r_B = 0.4, r_T = 0.5, \beta = \pi/6, vrel0 = 23$
7	$r_B = 0.5, r_T = 0.5, \beta = \pi/3, vrel0 = 0.5293$
8	$r_B = 0.6, r_T = 0.3, \beta = \pi/3, vrel0 = 0.5293$
9	$r_B = 0.5, r_T = 0.4, \beta = \pi/3, vrel0 = 0.5293$
10	$r_B = 0.4, r_T = 0.5, \beta = \pi/3, vrel0 = 23$

Table 2: Different combinations of restitution coefficients and angles of capsule incline

#### 3.1 Influence of restitution coefficients $r$ under $\beta = \pi/6$

By translating the formulae in Section 2 into Matlab code, we can output bifurcation diagram revealing the relative velocity and harvested energy with respect to the capsule length  $d$  under different initial conditions. In this subsection, the angle of capsule incline  $\beta$  has always been  $\pi/6$ .

Firstly, consider the case in which symmetric restitution coefficients  $r_B = r_T = 0.5$  and the initial conditions  $\phi = 6.18$ ,  $vrel0 = 0.5293$ . The bifurcation diagrams are shown in Fig.2.

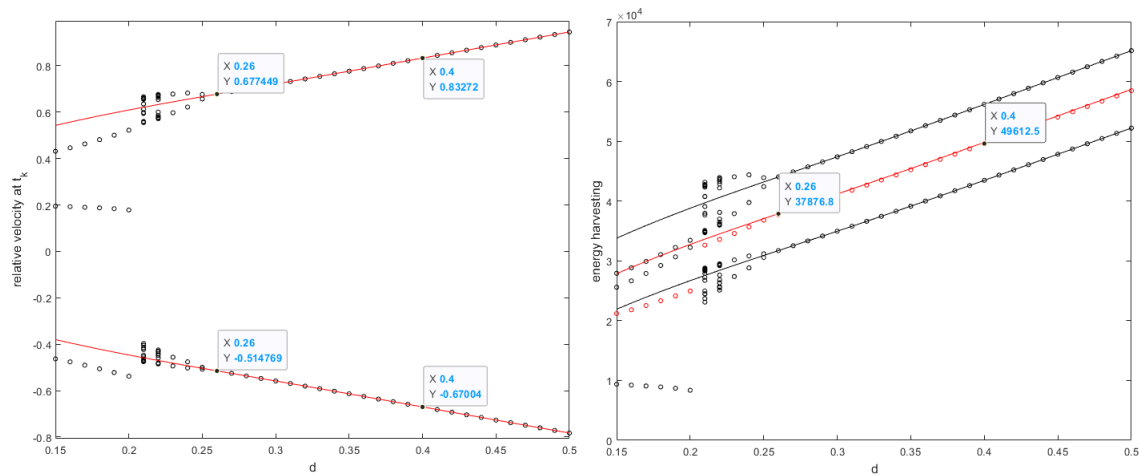


Figure 2:  $r_B = 0.5, r_T = 0.5, \beta = \pi/6, vrel0 = 0.5293$

Fig.3 contains bifurcation diagrams with asymmetric restitution coefficients  $r_B = 0.6, r_T =$

0.3 and initial conditions  $\phi_0 = 6.18$ ,  $v_{rel0} = 0.5293$ .

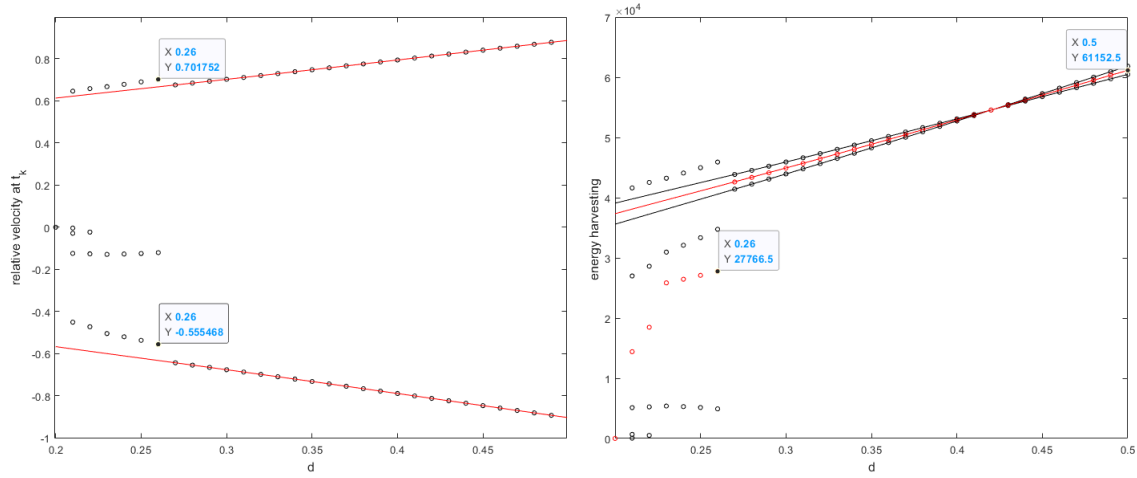


Figure 3:  $r_B = 0.6$ ,  $r_T = 0.3$ ,  $\beta = \pi/6$ ,  $v_{rel0} = 0.5293$

Then exchange values of  $r_B$  and  $r_T$ , keeping the other parameters the same. When the code began to run, the strange behaviors of the phase portrait and time series of the displacement indicate it is a chaotic motion. Since the restitution coefficient at the bottom ( $r_B = 0.3$ ) is much less than that at the top ( $r_T = 0.6$ ), the initial velocity  $v_{rel0}$  can not transport the ball successfully from the bottom to the top, so  $v_{rel0}$  is increased to 67 to provide a greater initial velocity.

In Fig.4, when  $d < 0.2$ , there exist some short intervals with relative velocity approaching to 0 so that very little energy is produced, which can be interpreted as motion restabilization.

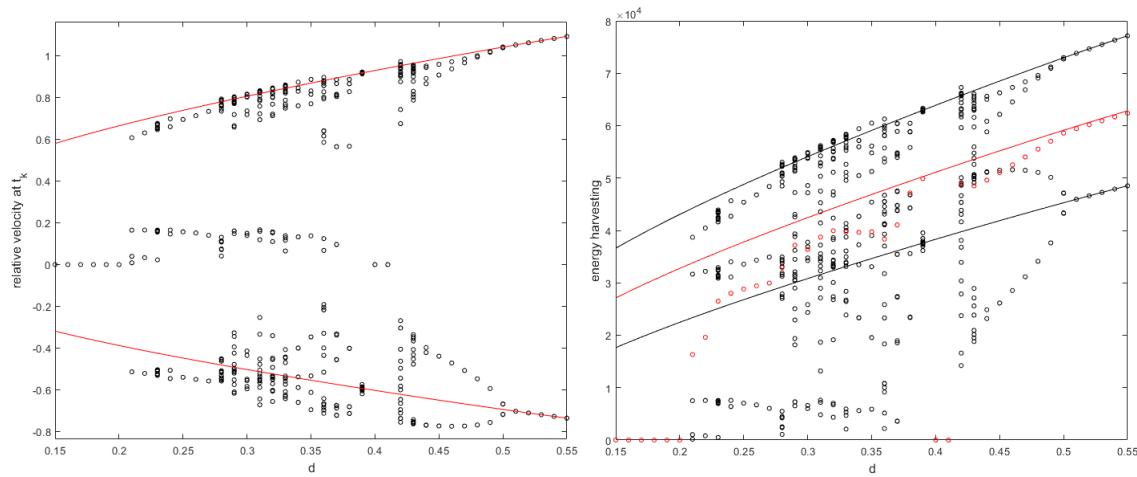
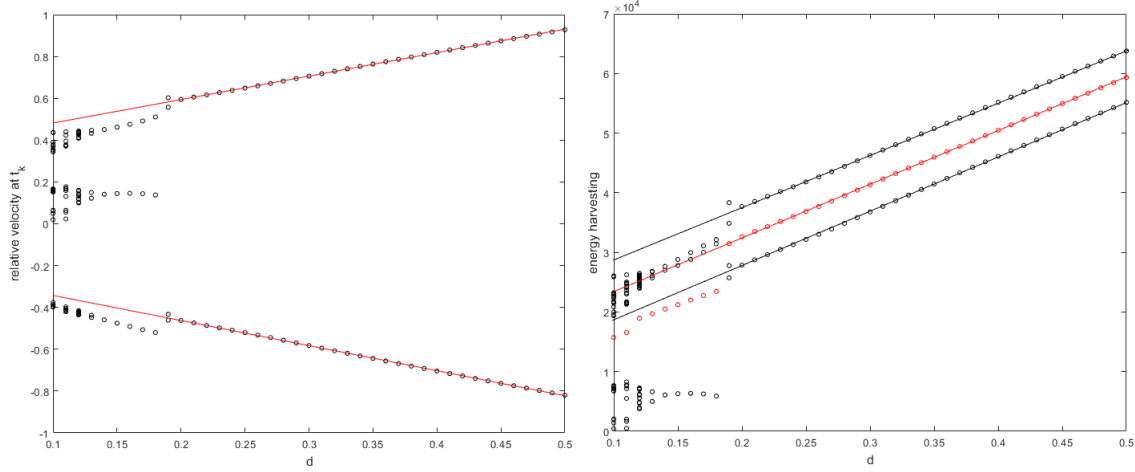
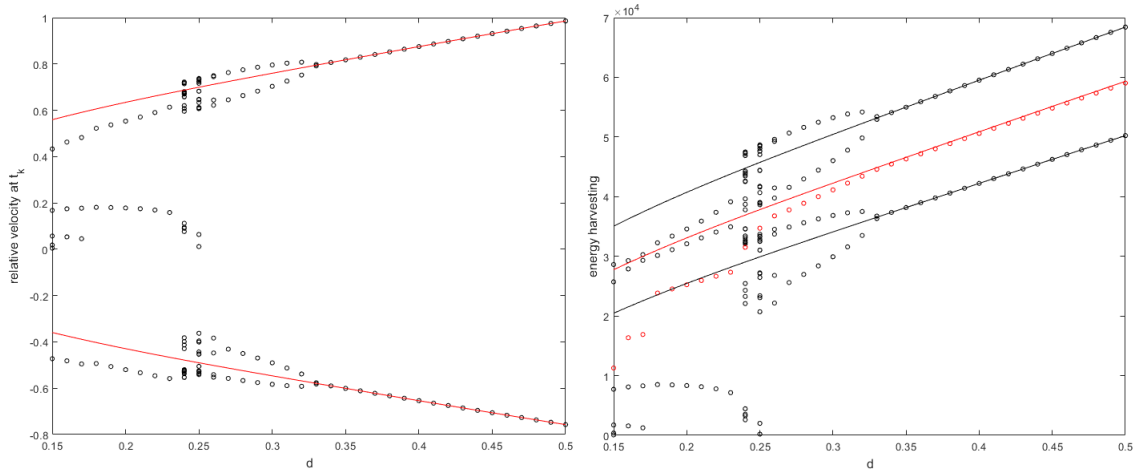


Figure 4:  $r_B = 0.3$ ,  $r_T = 0.6$ ,  $\beta = \pi/6$ ,  $v_{rel0} = 67$

Figure 5:  $r_B = 0.5$ ,  $r_T = 0.4$ ,  $\beta = \pi/6$ ,  $v_{rel0} = 0.5293$ 

Similarly, in Fig.6, the value of initial velocity  $v_{rel0}$  still needs to be adjusted from 0.5293 to 23 when  $r_B = 0.4$  and  $r_T = 0.5$  to avoid a chaotic motion.

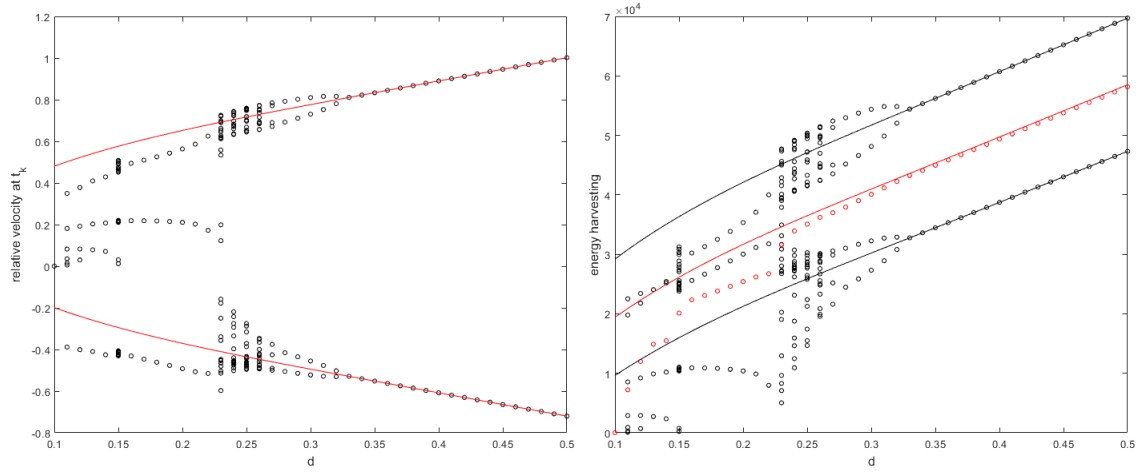
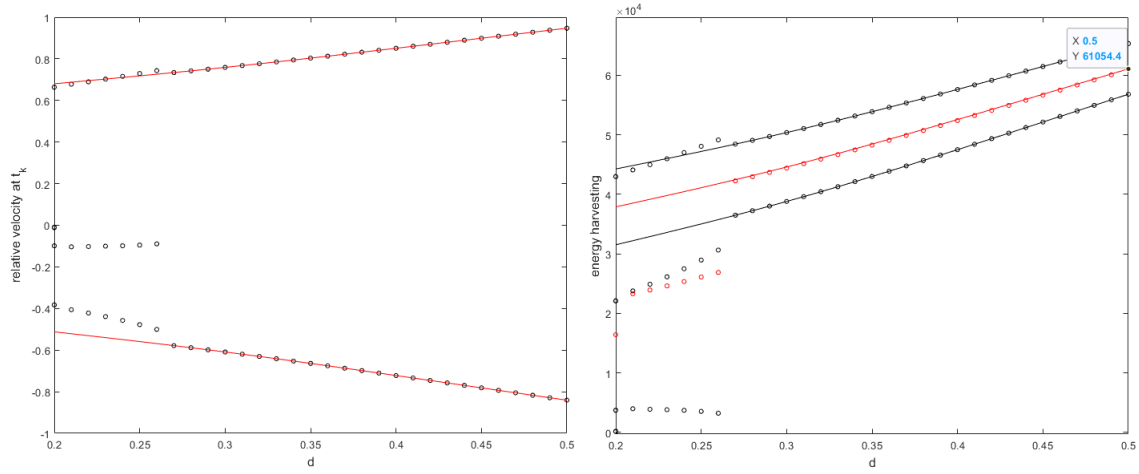
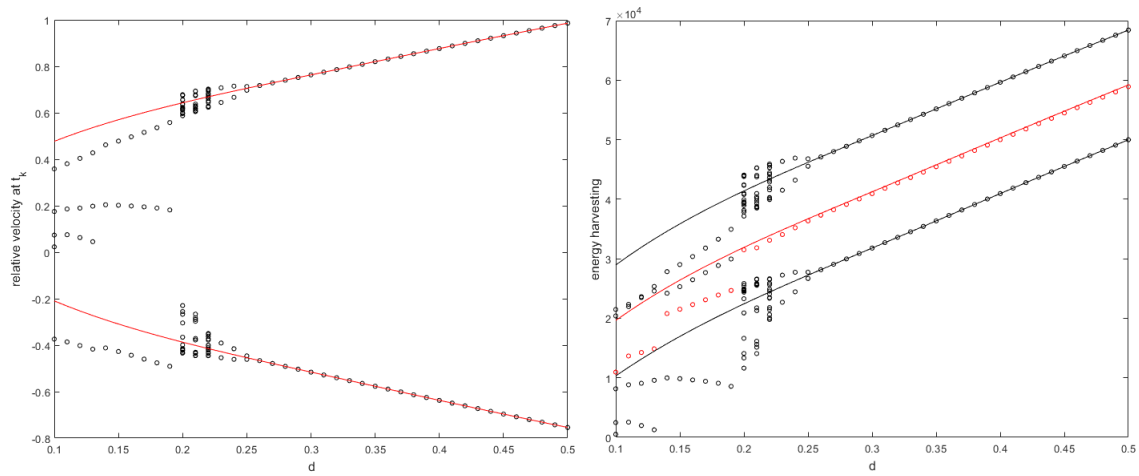
Figure 6:  $r_B = 0.4$ ,  $r_T = 0.5$ ,  $\beta = \pi/6$ ,  $v_{rel0} = 23$ 

In general, by keeping  $\beta = \pi/6$  the same and choosing different combinations of  $r_B$  and  $r_T$ , bifurcation diagrams above (Fig.2 - Fig.6) show that as capsule length  $d$  increases from 0.1 to 0.5, one branch of the analytic solutions about relative velocity increases in the range of  $(0.4, 1)$ , while another branch decreases in the range of  $(-0.8, -0.2)$ .

As for the graph of energy harvesting, with the increase of the capsule length  $d$ , the average output voltage  $U_{ave}$  (red empty circles and red solid lines) increases. No matter what value  $U_{ave}$  starts at, the output voltages all end up around  $6 \times 10^4 V$  at  $d = 0.5$ .

### 3.2 Influence of angle of capsule incline $\beta$

In this subsection, we only change the angle of capsule incline  $\beta$  from  $\pi/6$  to  $\pi/3$  and generate the following figures corresponding to the last subsection.

Figure 7:  $r_B = 0.5$ ,  $r_T = 0.5$ ,  $\beta = \pi/3$ ,  $v_{rel0} = 0.5293$ Figure 8:  $r_B = 0.6$ ,  $r_T = 0.3$ ,  $\beta = \pi/3$ ,  $v_{rel0} = 0.5293$ Figure 9:  $r_B = 0.5$ ,  $r_T = 0.4$ ,  $\beta = \pi/3$ ,  $v_{rel0} = 0.5293$

Here in Fig.10 with parameters  $r_B = 0.4$ ,  $r_T = 0.5$ ,  $\beta = \pi/3$ , the initial velocity  $v_{rel0}$  still needs to be set as 23 instead of 0.5293. As the angle of incline increased from  $\pi/6$  to  $\pi/3$ , the ball needs a larger initial velocity to counteract gravity.

Just like the behavior in Fig.4, motion restabilization causes the relative velocity and harvested energy to approach 0 over some interval like  $(0.3, 0.38)$ .

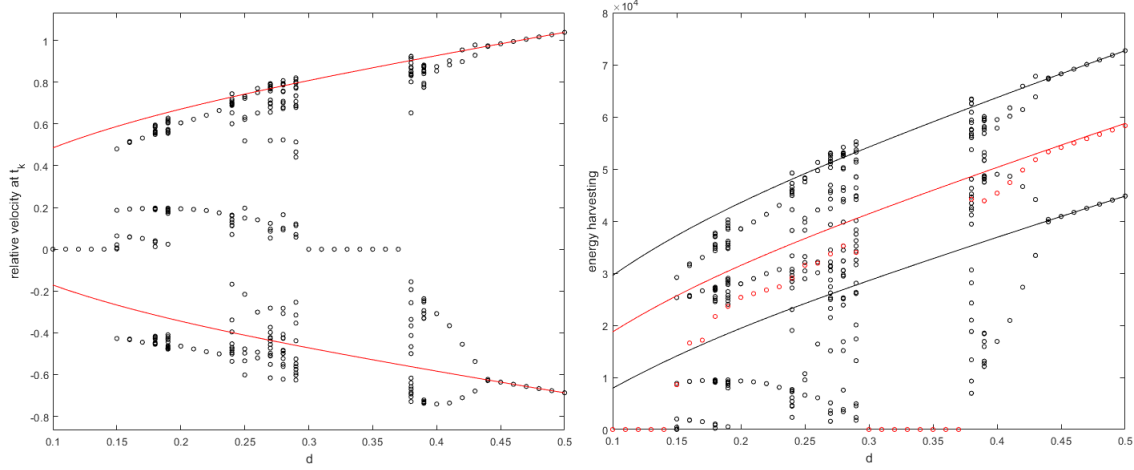


Figure 10:  $r_B = 0.4$ ,  $r_T = 0.5$ ,  $\beta = \pi/3$ ,  $v_{rel0} = 23$

By comparing the corresponding figures (Fig.2 and Fig.7, Fig.3 and Fig.8, Fig.5 and Fig.9, Fig.6 and Fig.10), it can be found that under the same combination of restitution coefficients, angles of capsule incline make little difference in the amount of energy harvesting.

In addition, the same statement that although the output voltage  $U_{imp} - U_{in}$  at the top and bottom impacts are farther apart for larger angles of inclination, the mean voltage  $U_{ave}$  takes similar values for different  $\beta$  is gotten as in the case of symmetric restitution coefficients ([Serdukova et al. \(2021\)](#)).

Based on the conclusions drawn from Section 3.1 and 3.2 with respect to the influence of restitution coefficients and angle of capsule incline, it can be demonstrated that in most cases, average output voltage  $U_{ave}$  cannot exceed  $6 \times 10^4 V$ , except when  $r_B = 0.6$ ,  $r_T = 0.3$ , the average output voltage  $U_{ave}$  reaches  $61152.5 V$  ( $\phi = \frac{\pi}{6}$ ) at  $d = 0.5$ , which can be regarded as the optimal combination of parameters to achieve the maximum energy output.

## 4 Different behaviors of bifurcation diagrams

We focus on the case in Fig.3 ( $r_B = 0.6$ ,  $r_T = 0.3$ ,  $\beta = \pi/6$ ,  $v_{rel0} = 0.5293$ ) which produces the maximum amount of energy to examine the different behaviors of bifurcation diagram. Fig.11 is the bifurcation diagram revealing the relationship between relative velocity and phase shift  $\phi$  of the  $k$ th impact with respect to the capsule length  $d$ . Some typical points representing 1-1 T-periodic motion and 2-1 T-periodic motion are picked out as initial conditions and the codes are run again with  $t_{final} = 10$ . Then the phase portraits and velocity time series about two kinds of motion are discussed to find what is happening in

the capsule.

In Fig.11, when  $d = 0.33$ , the corresponding velocity is 0.729028 and  $\phi$  is 1.21387, which represents 1-1 T-periodic motion. In terms of 2-1 T-periodic motion, the point with  $d = 0.25$ ,  $v = 0.689829$ ,  $\phi = 0.922985$  is discussed.

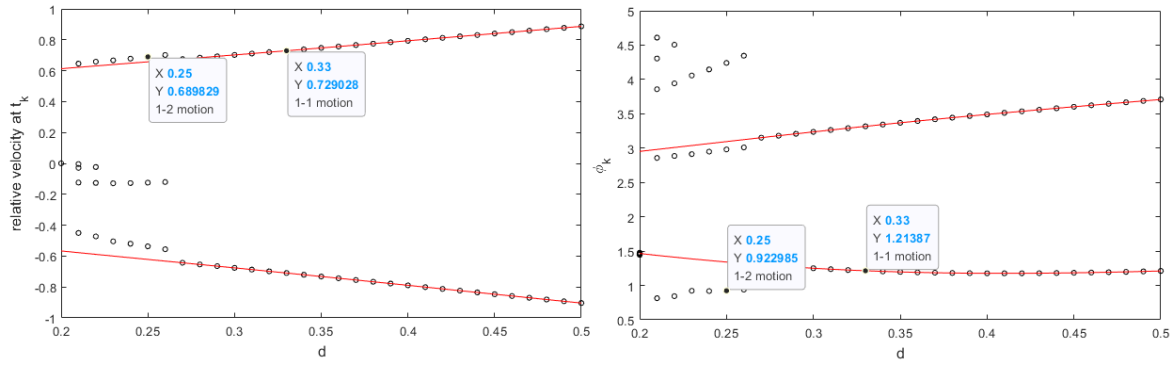


Figure 11: Bifurcation diagram about relative velocity and  $\phi$

#### 4.1 1-1 T-periodic motion

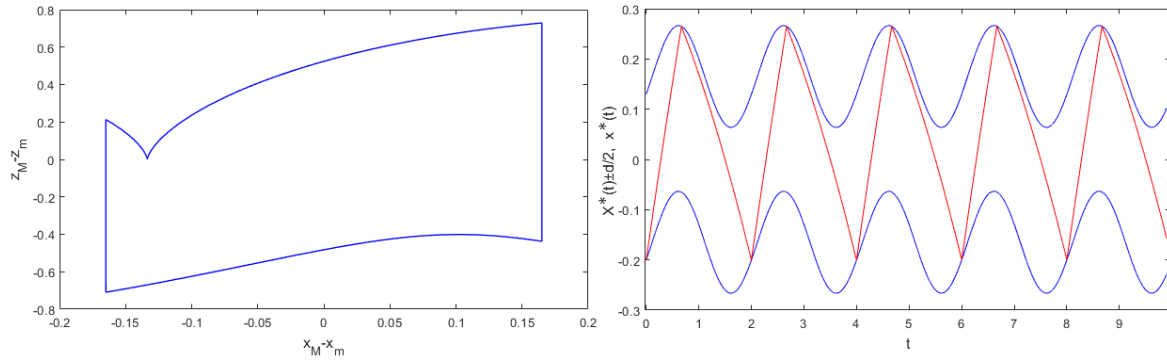


Figure 12: Initial conditions:  $ss(d) = 0.33$ ,  $vrel0(\dot{z}) = 0.729028$ ,  $phi0(\phi) = 1.21387$

The phase portrait on the left shows that on the bottom of the capsule, there is one impact happened between  $(-0.2, -0.15)$ . Analogously, in the range of  $(0.15, 0.2)$ , there is an impact on the top of the capsule.

As for the time series of displacement of capsule (blue solid lines) and ball (red solid lines) on the right, the impact is periodic over time with one impact on the bottom and one on the top of the capsule.

## 4.2 2-1 T-periodic motion

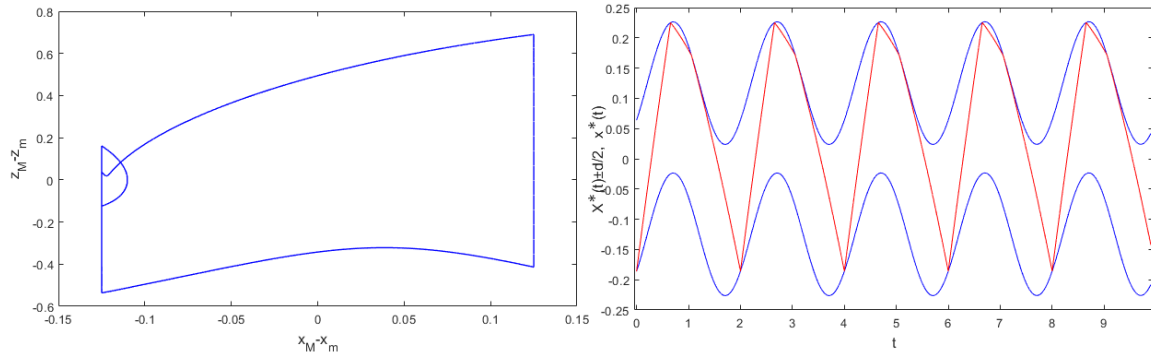


Figure 13: Initial conditions:  $ss(d) = 0.25$ ,  $vrel0(\dot{z}) = 0.689829$ ,  $phi0(\phi) = 0.922985$

In the phase portrait on the left, there are twice change of the velocity happened in the domain  $(-0.15, -0.1)$ , which corresponds to two impacts on the bottom of the device. On the top, only one impact occurs just like in 1-1 T-periodic motion.

In the time series graph, there are two intersections between the displacement of capsule (upper blue solid curve) and that of the ball (red lines) and one intersection between the lower blue solid curve and the red line, which represents two impacts on the bottom and one impact on the top.

## 5 Conclusions

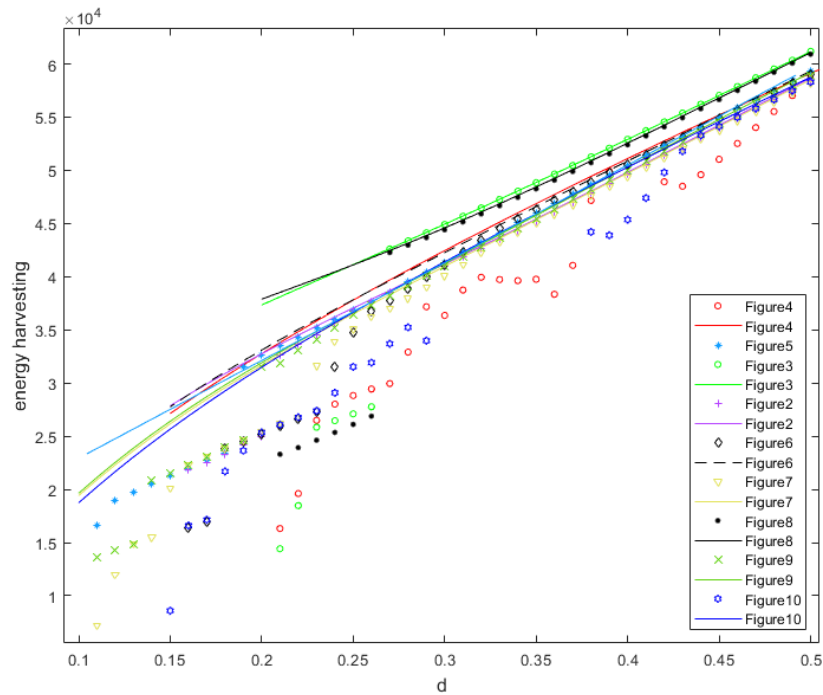


Figure 14: Comparison of energy harvesting of all figures

The paper uses the vibro-impact energy harvester with asymmetric restitution coefficients as the model. The membrane made of special material - dielectric elastomer can quantify the output energy well. On this basis, we parameterize the coefficients, extract the analytic solutions from the model, conduct linear stability analysis, then compile the formulae into the Matlab code, and finally mine the typical behaviors of the ball from the output graphs. Through numerical simulations, bifurcation diagrams, phase portraits and time series for velocity are produced. According to the results of calculation and analysis from an analytical and numerical perspective, we summarize these conclusions:

- This vibro-impact energy harvesting system has both both benefits and limitations. It can help us observe a wide range of rich nonlinear phenomena. Another advantage is that it is conservative and keeps a constant energy level between each impact. As for the limitation of the design, most of the derived maps such as bifurcation diagrams and phase portraits can not be solved explicitly, which can only be treated semi-analytically and numerically.
- With appropriate parameter combination, asymmetry can provide more efficient energy output than symmetry like Fig.3 (61152.5V) showing improved performance compared with Fig.2 ( $< 60000V$ ).
- When the restitution coefficient on the bottom  $r_B$  is not large enough (e.g.  $r_B < 0.5 < r_T$ ) to give the ball enough initial velocity to reach the top of the capsule, the value of initial velocity  $v_{rel0}$  should be increased (e.g. from 0.5293 to 23).
- As capsule length  $d$  increases over the interval (0.1, 0.5), one branch of the analytic solutions about relative velocity increases from 0.4 to 1 while another branch decreases from  $-0.2$  to  $-0.8$ . With the increase of the capsule length  $d$ , the average output voltage  $U_{ave}$  in every figure increases gradually.
- Although the output voltage  $U_{imp} - U_{in}$  at the top and bottom impacts are farther apart for larger angles of inclination, the average output voltage  $U_{ave}$  takes similar values for different  $\beta$  and ends at around  $6 \times 10^4 V$  at  $d = 0.5$ .
- Energy output are not only dependent on the ratio of the restitution coefficients, but also on their magnitude, combined with the angle of incline of the device. Under the same combination of restitution coefficients, angles of capsule incline make little difference. The amount of collected energy depends more on the combinations of asymmetric coefficients than the angle of capsule incline.

All the average output voltages  $U_{ave}$  mentioned in the above energy harvesting diagrams from Fig.2 - Fig.10 are combined into Fig.14. Compared with other analytical solutions,



Fig.3 and Fig.8 have obvious advantages in energy harvesting over the whole interval. Both two figures share the same restitution coefficients  $r_B = 0.6$  and  $r_T = 0.3$ , but with different angles of capsule incline. Therefore this parameter combination is considered as the optimal energy harvester that can harvest maximum energy with average output voltage  $U_{ave} = 61054.4V$  ( $\phi = \frac{\pi}{3}$ ) and  $U_{ave} = 61152.5V$  ( $\phi = \frac{\pi}{6}$ ) at  $d = 0.5$ .

In the selection of parameters  $r_B$ ,  $r_T$  and  $\beta$ , this paper only discusses some representative discrete data in Table 2, so our conclusions are not general enough. In future work, we would like to construct some continuous forms combined with each parameter like the ratio of  $r_B$  and  $r_T$  ( $\frac{r_B}{r_T}$ ) to strive for a more comprehensive, rigorous analysis and convert derived maps from semi-analytical to analytical solutions. We can also consider the influence of other parameters like the forcing amplitude  $A$  ( $A = 1$  in our discussion), perform further analytical calculations and explore more precise conditions to constrain the coefficients, and further search for the best device design for maximum energy output.

## 6 Bibliography

- Chernous' Ko, F. (2002), 'The optimum rectilinear motion of a two-mass system', *Journal of applied Mathematics and Mechanics* **66**(1), 1–7.
- Dulin, S., Lin, K., Serdukova, L., Kuske, R. & Yurchenko, D. (2022), 'Improving the performance of a two-sided vibro-impact energy harvester with asymmetric restitution coefficients', *International Journal of Mechanical Sciences* **217**, 106983.  
**URL:** <https://www.sciencedirect.com/science/article/pii/S0020740321006901>
- Glass, P., Cheung, E. & Sitti, M. (2008), 'A legged anchoring mechanism for capsule endoscopes using micropatterned adhesives', *IEEE Transactions on Biomedical Engineering* **55**(12), 2759–2767.
- Graf, C., Hitzbleck, J., Feller, T., Clauberg, K., Wagner, J., Krause, J. & Maas, J. (2014), 'Dielectric elastomer-based energy harvesting: Material, generator design, and optimization', *Journal of Intelligent Material Systems and Structures* **25**(8), 951–966.
- Pelrine, R., Kornbluh, R. D., Eckerle, J., Jeuck, P., Oh, S., Pei, Q. & Stanford, S. (2001), Dielectric elastomers: generator mode fundamentals and applications, in 'Smart Structures and Materials 2001: Electroactive Polymer Actuators and Devices', Vol. 4329, pp. 148–156.
- Serdukova, L., Kuske, R. & Yurchenko, D. (2021), 'Post-grazing dynamics of a vibro-impacting energy generator', *Journal of Sound and Vibration* **492**, 115811.  
**URL:** <https://www.sciencedirect.com/science/article/pii/S0022460X20306404>
- Strogatz, S. H. (2018), *Nonlinear dynamics and chaos with Applications to Physics, Biology, Chemistry, and Engineering*, CRC Press Taylor and Francis Group.
- Valdastri, P., Webster, R. J., Quaglia, C., Quirini, M., Menciassi, A. & Dario, P. (2009), 'A new mechanism for mesoscale legged locomotion in compliant tubular environments', *IEEE Transactions on Robotics* **25**(5), 1047–1057.

Yurchenko, D., Lai, Z., Thomson, G., Val, D. V. & Bobryk, R. V. (2017), ‘Parametric study of a novel vibro-impact energy harvesting system with dielectric elastomer’, *Applied Energy* **208**, 456–470.

Yurchenko, D., Val, D. V., Lai, Z., Gu, G. & Thomson, G. (2017), ‘Energy harvesting from a de-based dynamic vibro-impact system’, *Smart Materials and Structures* **26**(10), 105001.

## A Appendix

The detailed steps of the calculation about eigenvalues of the matrix  $DP$  are attached below. The entries of the matrices in (18) are

$$\begin{aligned}
 \frac{\partial t_{k+1}}{\partial t_k} &= \frac{r_B \dot{Z}_k - \bar{g}T_1 - f(t_k)T_1}{r_B \dot{Z}_k - \bar{g}T_1 - F_1(t_{k+1}) + F_1(t_k)}, \\
 \frac{\partial t_{k+1}}{\partial \dot{Z}_k} &= \frac{-r_B T_1}{r_B \dot{Z}_k - \bar{g}T_1 - F_1(t_{k+1}) + F_1(t_k)}, \\
 \frac{\partial \dot{Z}_{k+1}}{\partial t_k} &= \frac{\partial t_{k+1}}{\partial t_k} [f(t_{k+1}) + \bar{g}] - [f(t_k) + \bar{g}], \\
 \frac{\partial \dot{Z}_{k+1}}{\partial \dot{Z}_k} &= -r_B + \frac{\partial t_{k+1}}{\partial \dot{Z}_k} [f(t_{k+1}) + \bar{g}],
 \end{aligned} \tag{20}$$

$$\begin{aligned}
 \frac{\partial t_{k+2}}{\partial t_{k+1}} &= \frac{r_T \dot{Z}_{k+1} - \bar{g}T_2 - f(t_{k+1})T_2}{r_T \dot{Z}_{k+1} - \bar{g}T_2 - F_1(t_{k+2}) + F_1(t_{k+1})}, \\
 \frac{\partial t_{k+2}}{\partial \dot{Z}_{k+1}} &= \frac{-r_T T_2}{r_T \dot{Z}_{k+1} - \bar{g}T_2 - F_1(t_{k+2}) + F_1(t_{k+1})}, \\
 \frac{\partial \dot{Z}_{k+2}}{\partial t_{k+1}} &= \frac{\partial t_{k+2}}{\partial t_{k+1}} [f(t_{k+2}) + \bar{g}] - [f(t_{k+1}) + \bar{g}], \\
 \frac{\partial \dot{Z}_{k+2}}{\partial \dot{Z}_{k+1}} &= -r_T + \frac{\partial t_{k+2}}{\partial \dot{Z}_{k+1}} [f(t_{k+2}) + \bar{g}].
 \end{aligned} \tag{21}$$

For periodic motion with  $T = 2$  the trace and determinant of the matrix  $DP$  in (18) are

$$\begin{aligned}
 Tr(DP) &= \frac{1}{\epsilon_1 \epsilon_2} [r_B + r_B T_1 (f(t_{k+1}) + \bar{g})] \cdot [r_T - r_T T_2 (f(t_k) + \bar{g})] - \frac{\epsilon_3 \epsilon_4}{\epsilon_1 \epsilon_2} \\
 &\quad - \frac{r_T T_2}{\epsilon_2} [f(t_k) + \bar{g} + \frac{\epsilon_4}{\epsilon_1} (f(t_{k+1}) + \bar{g})] + \frac{r_B T_1}{\epsilon_1} [f(t_{k+1}) + \bar{g} - \frac{\epsilon_3}{\epsilon_2} (f(t_k) + \bar{g})],
 \end{aligned} \tag{22}$$

$$Det(DP) = \frac{r_B^2 r_T^2 \dot{Z}_k}{F_1(t_k) - F_1(t_{k+1}) + r_T F_1(t_k) - r_T F_1(t_{k+1}) + \bar{g}T_2 - \bar{g}r_T T_1 + \dot{Z}_k r_B r_T}, \tag{23}$$

where  $\epsilon_1 = F_1(t_k) - F_1(t_{k+1}) + \dot{Z}_k r_B - \bar{g}T_1$ ,  $\epsilon_2 = F_1(t_k) - F_1(t_{k+1}) + \bar{g}T_2 + r_T \epsilon_1$ ,  $\epsilon_3 = f(t_{k+1})T_2 + \bar{g}T_2 + r_T \epsilon_1$  and  $\epsilon_4 = f(t_k)T_1 + \bar{g}T_1 + \dot{Z}_k r_B$ .